

Moment magnitude estimates for Central Anatolian earthquakes using coda waves

Tuna Eken¹

¹*Department of Geophysical Engineering, the Faculty of Mines, Istanbul Technical University, 34469 Maslak, Sarıyer, Istanbul, Turkey*

Abstract

Proper estimate of moment magnitude that is a physical measure of the energy released at earthquake source is essential for better seismic hazard assessments in tectonically active regions. Here a coda wave modeling approach that enables the source displacement spectrum modeling of examined event was used to estimate moment magnitude of central Anatolia earthquakes. To achieve this aim, three component waveforms of local earthquakes with magnitudes $2.0 \leq M_L \leq 5.2$ recorded at 72 seismic stations which have been operated between 2013 and 2015 within the framework of the CD-CAT passive seismic experiment.

An inversion on the coda wave traces of each selected single event in our database was performed in five different frequency bands between 0.75 and 12 Hz. Our resultant moment magnitudes (M_W -coda) exhibit a good agreement with routinely reported local magnitude (M_L) estimates for study area. Finally, we present an empirical relation between M_W -coda and M_L for central Anatolian earthquakes.

Keyword(s): Coda waves modelling, seismic moment, moment magnitude, Radiative Transfer Theory

1. Introduction

The robust and stable knowledge of source properties (e.g. moment magnitude estimates) is crucial in seismically active countries such as Turkey for a better evaluation of seismic hazard potential as this highly depends on establishment of reliable seismicity catalogs. Moreover, accurate information on source parameters could be important when developing regional attenuation properties.

Conventional type of magnitude scales (M_L , m_b , M_S) as the result of empirically derived using direct wave analyses can be biased due to various effects such as source radiation pattern, directivity, and heterogeneities along the path since they may cause drastic changes in direct wave amplitude measurements (e.g., Favreau and Archuleta, 2003). Instead several early studies depending on the analysis of local and/or regional coda envelopes have indicated that coda wave amplitudes are significantly less variable by a factor of 3-to-5 compared to direct wave amplitudes (e.g., Mayeda and Walter, 1996; Mayeda et al., 2003; Eken et al., 2004; Malagnini et al., 2004; Gök et al., 2016). In fact local or regional coda waves that are usually considered to be generally ~~to be~~ composed of scattered waves and can be simply explained by that sample the single scattering model of Aki (1969) have been proven to be virtually insensitive to any source radiation pattern effect in contrast to direct waves because of the volume averaging property of the coda waves sampling the entire focal sphere (e.g., Aki and Chouet, 1975; Rautian and Khalturin, 1978). In Sato and Fehler (1998) and Sato et al. (2012) an extensive review study on the theoretical background of coda generation and advances of empirical observations and modelling efforts can be found in details.

Vanability is visible in the early coda

There have been several approaches used for extracting information on earthquake source size via coda wave analyses. These approaches can be mainly divided into two groups. The first

group of studies employs coda normalization strategy in which measurements require a correction for seismic attenuation parameters (e.g. intrinsic and scattering) that can be described by some empirical quality factors. To calibrate final source properties reference events are used to adjust measurements with respect to each other. For forward generation of synthetic coda envelopes, either single-backscattering or more advanced multiple-backscattering approximation are used. An example to this group is an empirical method originally developed by Mayeda et al. (2003) to investigate seismic source parameters such as energy, moment, and apparent stress drop in the western United States and in Middle East. They corrected observed coda envelopes for various influences, for instance, path effect, S-to-coda transfer function, site effect, and any distance-dependent changes in coda envelope shape. Empirical coda envelope method have been successfully applied to different regions with complicated tectonics such as northern Italy (e.g. Morasca et al., 2008), Turkey and Middle East (e.g. Eken et al., 2004; Gök et al. 2016); or Korean Peninsula (e.g. Yoo et al., 2013).

Parametric approach

Second type of approach is a joint inversion technique that is based on a simultaneous optimization of source, path, and site specific terms via synthetic and observed coda envelope fitting within a selected time window including observed coda and direct-S wave parts. In this approach, the Radiative Transfer Theory (RTT) is employed for analytic expression of synthetic coda wave envelopes. The method that does not rely on coda normalization strategy was originally developed by Sens-Schönfelder and Wegler (2006) and successfully tested on local and regional earthquakes ($4 \leq M_l \leq 6$) detected by the German Regional Seismic Network. Further it has been applied to investigate source and frequency dependent attenuation properties of different geological settings, i.e., Upper Rhine Graben and Molasse Basin regions in Germany and western Bohemia/Vogtland in Czechia (Eulenfeld and Wegler,

Physics based approach

2016); entire United States (2017); central and western North Anatolian Fault Zone (Gaebler et al., 2018; Izgi et al., 2018). A more realistic earth model in which anisotropic scattering conditions were earlier considered by Gusev and Abubakirov (1987) yielded peak broadening effects of the direct seismic wave arrivals. This approach later was used in previous studies (e.g. Zeng, 1993; Przybilla and Korn, 2008; Gaebler et al., 2015) that dealt with propagation of P-wave elastic energy and the effect of conversion between P- and S-wave energies. ~~X~~

English

In the current work I present estimated source spectra as an output of a joint inversion of S- and coda waves parts of local earthquake waveforms 487 local earthquakes with magnitudes 2.0 < ML < 4.5 detected in central Anatolia for their source parameters. The approach used here employs isotropic acoustic RTT approach for forward calculation of synthetic coda envelopes. Gaebler et al. (2015) ^{ve} has observed that modeling results from isotropic scattering were almost comparable with those inferred from relatively more complex elastic RTT simulations with anisotropic scattering conditions. The use of a joint inversion technique is advantageous since it is insensitive to any potential bias, which could be introduced by external information, i.e., source properties of a reference that is obtained separately from other methods for calibration. This is mainly because of the fact that we utilize an analytical expression of physical model involving source, and path related parameters to describe the scattering process. Moreover the type of optimization during joint inversion enables the estimates for source parameters of relatively small sized events compared to the one used in coda-normalization methods.

English

What about trade-off between parameters?

2. Regional Setting ~~and Data~~

Present tectonic setting of Anatolia and surrounding regions have been mainly outcome of the northward converging movements among Africa, Arab, and Eurasian plates. To the west, subducting African plate with a slab roll-back dynamics beneath Anatolia along Hellenic Trench has led to back-arc extension in the Aegean and western Anatolia, while compressional deformation to the east around the Bitlis–Zagros suture was explained by collisional tectonics (e.g. Taymaz et al., 1990; Bozkurt, 2001). Westward extrusion of Anatolian plate controlled by these plate motions, in consequence, has been accommodated through two conjugate strike-slip fault zones separating the Anatolian and Arabian from Eurasian plates: 1600 km long east-west striking transform plate boundary, North Anatolian fault zone (NAFZ), and northeast-southwest–striking East Anatolian fault zone (EAFZ) (Fig. 1). These neotectonic features could have easily traced the weakness zones along the boundaries of amalgamated continental fragments that have developed following the closure of Tethys Ocean (Şengör et al., 2005).

Central Anatolia is located between extensional regime to the west due to the subduction, and compressional regime tectonics to the east due to the collisional tectonics. The major fault zone in the region, the Central Anatolian Fault Zone (CAFZ) (Fig. 2), which primarily represents a transtensional fault structure with small amount of left-lateral offset during the Miocene (e.g. Koçyiğit and Beyhan, 1998), can be considered as a boundary between the carbonate nappes of the Anatolide-Tauride block from the highly deformed and metamorphosed rocks in the Kırşehir block. However recent studies that have reported significant lateral variations in seismic wave speeds (e.g. Fichtner et al., 2013a,b; Delph et al., 2015) and Bouguer gravity (Ateş et al., 1999) across the fault implied that a progressive relative movement along the faults would result in sharp difference in crust and mantle

English

126 structures. New findings on structural, geomorphic, and geochronologic data collected from
127 several segments along the CAFZ were interpreted that the transtensional type deformation
128 has reactivated paleotectonic structures and finally accommodated E-W extension due to the
129 westward extrusion of Anatolia (Higgins et al., 2015). To the northwest of the CAFZ, Tuz
130 Gölü Fault Zone (TGFZ) (Fig. 2), which is characterized by a right-lateral strike slip motion
131 with a significant oblique-slip normal component, appears to be collocated with Tuz Gölü
132 Basin sedimentary deposits as well as crystalline rocks within Kırşehir Block (e.g. Çemen et
133 al., 1999; Bozkurt et al., 2001; Taymaz et al., 2004). Present day crustal deformation and state
134 of stress related to the TGFZ have been reported in Çubuk et al. (2014) via observed
135 earthquake cluster activity reaching depths of 5-6 km with magnitudes up to $M_L 5.6$ in the
136 Bala region (between 2005 and 2007) located ~~at~~ the north of the TGFZ (Çubuk et al., 2014).

137 English
138 At the southwest tip of the study region, the EAFZ generates large seismic activity that can be
139 identified rather complicated seismotectonic setting: predominantly left-lateral strike-slip
140 motion correlated well with the regional deformation pattern but also existing local clusters of
141 thrust and normal faulting events on NS- and EW-trending subsidiary faults, respectively
142 (Bulut et al., 2012). [Such complicated behavior explains kinematic models of the shear
143 deformation zone evolution.] This active left-lateral fault zone since the late Miocene–Pliocene
144 exhibits ^a ~20 km-wide shear deformation zone with an annual 6-10 mm/yr slip rate. It
145 connects to the NAFZ at the Karlıova Triple Junction (Bozkurt, 2001) and to the south splits
146 into various segments nearby the Adana Basin (Kaymakci et al., 2006) (Fig. 2). Toward the
147 south, the EAFZ reaches the Dead Sea Fault Zone (DSFZ) that has a key role in
148 accommodating northward relative motions of Arabian and African Plates with respect to
149 Eurasia.

which models?

Start New Section on Data

150 The present work utilizes three-component waveforms of local seismic activity detected at 72
151 broadband seismic stations (Fig. 2) that have been operated for 2 years between 2013 and
152 2015 within the framework of a temporary passive seismic experiment, the Continental
153 Dynamics–Central Anatolian Tectonics (CD-CAT) (Portner et al., 2018). We benefit from
154 revisited standard earthquake catalogue information (publicly available at
155 <http://www.koeri.boun.edu.tr>) to extract waveform data for a total of 2231 examined events
156 with station-event pair distance less than 120 km and focal depths less than 10 km. Most of
157 the detected seismic activity in the study area is associated to several fault zones in the region,
158 i.e., the EAFZ, CAFZ, DSFZ, TGFZ, etc. Here we note that selection of only local
159 earthquakes is to exclude possible biases, which may be introduced by Moho boundary
160 guided Sn-waves while upper crustal earthquakes are preferred in this study to exclude effect
161 of relatively large-scale heterogeneities on coda wave trains. Finally a visual inspection
162 conducted over all waveforms to ensure high-quality waveforms reduces our event number to
163 1193. Selected station and event distributions can be seen in Figure 2.

164 → I do not understand the relation

165 Observed waveforms were prepared at 5 different frequency bands with central frequencies at
166 0.75, 1.5, 3.0, 6.0, 12.0 Hz via a Butterworth band-pass filtering process. In the next step, we
167 applied Hilbert transform to filtered waveform data in order to obtain the total energy
168 envelopes. An average crustal velocity model was used to predict P and S wave onsets on
169 envelopes and then based on this information: (i) the noise level prior to the P-wave onset was
170 eliminated (ii) S-wave window was determined starting at 3s prior to and 7 s afterwards S-
171 wave onset as this allowed to include all direct S-wave energy, (iii) starting at the end of the
172 S-wave window, a coda window of 100s at maximum was determined. Length of coda
173 windows can be shorter when signal-to-noise ratio (SNR) is less than 2.5 or when the same

window consists of coda waves from two earthquakes, which can give rise to a decline in the envelope. We omit the earthquakes with less than 10 s of coda length from our database.

How many paths in total?

↓ ?

3. Method

We adopted an inversion procedure that was originally developed by Sens-Schönfelder and Wegler (2006) and later modified by Eulenfeld and Wegler (2016). The forward part, which involves calculation of energy density for a specific frequency band caused by an isotropic source, is expressed in Sens-Schönfelder and Wegler (2006) as follows:

$$E_{mod}(t, r) = WR(r)G(t, r, g)e^{-bt} \quad (1)$$

where $G(t, r, g)$ represents Green's function that includes scattered wave field as well as direct wave. W gives source term and it is frequency dependent. $R(r)$ indicates the energy site amplification factor and b is intrinsic attenuation parameter.

Possible discrepancy between predicted and observed energy densities for each event at each station with N_{ij} time samples (index k) in a specific frequency band can be minimized using:

$$\epsilon(g) = \sum_{i,j,k}^{N_S, N_S, N_{ij}} (\ln E_{ijk}^{obs} - \ln E_{ijk}^{mod}(g))^2 \quad (2)$$

N_E

Here, the number of stations (index i) and events (index j) are shown by N_S and N_E , respectively. Optimization of g will be achieved when

$$\ln E_{ijk}^{obs} = \ln E_{ijk}^{mod} \quad (3) \quad \text{or}$$

$$\ln E_{ijk}^{obs} = \ln G(t_{ijk}, r_{ijk}, g) + \ln R_i + \ln W_j - bt_{ijk} \quad (4)$$

Equation 4 simply define an overdetermined inversion problem with $\sum_{i,j} N_{ij}$ number equation systems and with $N_S + N_E + 1$ variables and thus b , R_i , and W_j can be solved via a least-squares technique. $\epsilon(g)$ can be defined as sum over the squared residuals of the solution.

Eulenfeld and Wegler (2016) present a simple recipe to perform inversion:

(i) Calculate Green's functions through the analytic approximation of the solution for 3-D isotropic radiative transfer (e.g. Paasschens 1997; Sens-Schönfelder and Wegler, 2006) by using fixed scattering parameters and minimize equation 4 to solve for b , R_i , and W_j via a weighted least-squares approach.

(ii) Calculate $\epsilon(g)$ using equation 2.

(iii) Repeat (i) and (ii) by selecting different g to find the optimal parameters g , b , R_i and W_j that finally minimize the error function ϵ .

In Fig. 3 an example for the minimization process that was applied at five different frequency band is displayed for one selected event at recorded stations of the CD-CAT project.

Minimization described above for different frequencies will yield unknown spectral source energy term, W_j as well as site response, R_i and attenuation parameters, b , and g . The present study deals with frequency dependency of W_j since this information can be later useful to obtain source displacement spectrum and thus seismic moment and moment magnitudes of analyzed earthquakes using the formula of the S -wave source displacement spectrum for a double-couple source in the far-field, which is given by Sato et al. (2012):

$$\omega M(f) = \sqrt{\frac{5\rho_0 v_0^5 W}{2\pi f^2}} \quad (5)$$

Define notation

219 The relation between the obtained source displacement spectrum and seismic moment value
220 was earlier described in Abercrombie (1995) by:

221
$$\omega M(f) = M_0 \left(1 + \left(\frac{f}{f_c} \right)^{\gamma n} \right)^{-\frac{1}{\gamma}} \quad (6)$$

222 where n is related to the high-frequency fall-off and γ is known as shape parameter that
223 controls the sharpness of spectrum at corner frequency between the constant level M_0 (low
224 frequency part) and the fall-off with f^{-n} (high frequency part). Taking ^{the} logarithm of equation 6
225 gives:

226
227
$$\ln \omega M(f) = \ln M_0 - \frac{1}{\gamma} \ln \left(1 + \left(\frac{f}{f_c} \right)^{\gamma n} \right) \quad (7)$$

228
229 Eq.7 describes an optimization problem of which data forms observed source displacement
230 spectrum and four source parameters, M_0 , γ , n , and f_c are the unknown model parameters that
231 can be resolved in a simultaneous least-squares inversion of ~~the~~ equation 7. Finally moment
232 magnitude, M_w can be calculated from modeled source parameters, seismic moment, M_0
233 using a formula given by Hanks and Kanamori (1979):

234
235
$$M_w = \frac{2}{3} \log_{10} M_0 - 6.07 \quad (8)$$

236
237

4. Results and Discussions

238

4.1 Coda wave source spectra

239 Figure 4 displays observed values of source spectra established by inserting ^{the} inverted spectral
240 source energy term W at each frequency in Eq. 5 for all analyzed events. Each curve in this
241 figure represents model spectrum estimate based on inversion procedure described in previous

No W is Figure 5

Where is Figure 4 discussed?

242 section. Modeled spectrum characteristics computed for 487 local earthquakes of which
243 lateral distribution is presented in Figure 2 suggest, in general, that we were able to obtain
244 typically expected source displacement spectrum with a flat region around the low frequency
245 limit and decaying behaviour above a corner frequency.

246
247 Owing to the multiple-scattering process within small scale heterogeneities that makes coda
248 waves gain an averaging nature, the variation in coda amplitudes due to differences in
249 radiation pattern and path effect are reduced (Walter et al., 1995; Mayeda et al., 2003).
250 Eulenfeld and Wegler (2016) found that radiation pattern would have only a minor influence
251 on the S-wave coda while it might disturb attenuation models inferred from the direct S-wave
252 analyses unless the station distribution relative to the earthquakes indicates a good azimuthal
253 coverage. A peak-like source function assumption for small earthquakes that are utilized in
254 the present work was earlier proven to be adequate in early application of the coda-wave
255 fitting studies (e.g. Sens-Schönfelder and Wegler, 2006; Gaebler et al., 2015; and Eulenfeld
256 and Wegler, 2016). I do not understand

257
258 Conventional approaches (e.g. Abercrombie, 1995; Kwiitek et al., 2011) to estimate source
259 parameters such as corner frequency, seismic moment, high-frequency fall-off through fitting
260 of observed displacement spectra observed at a given station in an inversion scheme could be
261 misleading since these methods usually: (i) assume a constant value of attenuation effect (no
262 frequency variation) defined by a factor $\exp(-\pi f t Q^{-1})$ over the spectrum, (ii) and assume
263 omega-square model with a constant high-frequency fall-off parameter, $n=2$. Following Sens-
264 Schönfelder and Wegler (2006) and Eulenfeld and Wegler (2016), however, we estimate
265 attenuation parameters (intrinsic and scattering) separately within a simultaneous inversion
266 procedure in which high-frequency fall-off parameter varies. This is fairly consistent with

267 early studies (e.g. Ambeh and Fairhead, 1991; Eulenfeld and Wegler, 2016) where significant
268 deviations from the omega square model ($n > 3$) were reported implying that the omega-square
269 model as a source model for small earthquakes must be reconsidered in its general
270 acceptance. In our case, the smallest event was with M_W -coda larger than 2.0, thus we had no
271 chance to make a similar comparison, ~~if~~ however, high-frequency fall-off parameters varied
272 from $n=0.5$ to $n=4$. A notable observation in the distribution of n was $n=2$ or $n=2.5$ would be
273 better ^{to} explain earthquakes with M_W -coda > 4.0 whereas the smaller magnitudes exhibited
274 more scattered pattern of variation in n . Eulenfeld and Wegler (2016) claimed that the use of
275 separate estimates of the attenuation or correction for path effect via empirically determined
276 Green's function would be better strategy in order to invert station displacement spectra for
277 source parameters. This is mainly because smaller earthquakes (with $n > 2$), in particular,
278 assuming omega-square model can distort the estimates of corner frequency and even seismic
279 moment especially in regions where Q is strongly frequency dependent. ~~and ??~~

281 4.2 Coda wave –derived magnitude vs. M_L catalogue magnitude

282 A scatter plot between catalogue magnitudes based on local magnitudes (M_L) and our coda-
283 derived magnitudes (M_W -coda) that are inferred from resultant frequency dependent source
284 displacement spectra and thus seismic moment (e.g. Eq. 8) is shown in Fig. 6. Such
285 comparison suggests an overall coherency between both types of magnitudes. This implies
286 ^{FLA} very simple model of a first-order approximation for S-wave scattering with isotropic acoustic
287 radiative transfer approach can be efficient to link the amplitude and decaying character of
288 coda wave envelopes to the seismic moment of the source.

A linear regression analyses performed between M_W -coda and M_L magnitudes (Fig. 5) resulted in an empirical formula that can be employed to convert local magnitudes into coda-derived moment magnitude calculation of local earthquakes in this region:

$$M_{W-coda} = 1.1655 \pm 0.0337 \times M_L - 0.7085 \pm 0.0128 \quad (9)$$

Apparent move-out in Fig. 5 and Eq. 9, presumably stems from the use of different magnitude scales for comparison. The consistency between coda-derived moment magnitude and local magnitude scales for the earthquakes with M_W -coda > 3.0 indicates that our non-empirical approach successfully worked in this tectonically complex region. We observed similar type of consistency in early studies that investigate source properties of local and regional earthquakes based on empirical coda methods with simple 1-D radially symmetric path correction (e.g. Eken et al., 2004; Gök et al., 2016). Observable outliers in Figure 5, for the events with less than M_W 3.5, however, can be attributed to the either possible biases on local magnitude values taken from the catalogue or small biases on our intrinsic (Q_i^{-1}) and scattering (Q_s^{-1}) attenuation terms. One another possible contribution to such mismatch might be associated to the influences of mode conversions between body and surface waves or surface-to-surface wave scattering (e.g. Wu & Aki 1985) that are not restricted to low frequencies (<1Hz) (Sens-Schönfelder and Wegler, 2006).

Wu & Aki discussed in his reference

5. Conclusions

This study provides an independent solution for estimating seismic source parameters such as seismic moment and moment magnitude for local earthquakes in central Anatolia without requiring *a priori* information on reference events with waveform modelling results to be used for calibration or *a priori* information on attenuation for path effect corrections. In this

This is not an outcome of his work

315 regard, the approach used here can be easy and useful tool for investigation of source
316 properties of local events detected at temporal seismic networks. Moreover, seismic moment
317 can be approximated via waveform modelling methods but due to the small-scale
318 heterogeneities of the media that waves propagate, it is often a hard task to establish Green's
319 function for small earthquake ($M_L < 3.5$). An analytical expression of energy density Green's
320 function in a statistical manner employed in the present work enables neglecting the
321 interaction of the small-scale inhomogeneities with seismic waves as this can be practical for
322 seismic moment calculations of small events that may pose source energy at high-frequency.
323 It is noteworthy to mention that our isotropic scattering assumption does not consider
324 anisotropic case, which could be valid for real media, but still provides a simple and effective
325 tool to define the transport for the anisotropic case since the estimated scattering coefficient
326 can be interpreted as transport scattering coefficient. An averaging over S-wave window
327 enables to overcome biases caused by using unrealistic Green's function (Gaebler *et al.*
328 2015). Since the present study mainly focuses on source properties of local earthquakes in the
329 study area, scattering and intrinsic attenuation properties that are other products of our coda
330 envelope fitting procedure will be examined in details within a future work. Finally, the
331 empirical relation developed between M_W -coda and M_L will be a useful tool for quickly
332 converting catalogue magnitudes to moment magnitudes for local earthquakes in the study
333 area.

334 *→ It could have been better in the conclusion*
335 *Data and resources*

*you mean: neglecting
non isotropic scattering?*

336 The python code used for carrying out the inverse modeling is available under the permissive
337 MIT license and is distributed at <https://github.com/trichter/qopen>. We are grateful to the IRIS
338 Data Management Center for maintaining, archiving and making the continuous broadband
339 data used in this study open to the international scientific community.

340

341 *Acknowledgement*

342 The facilities of IRIS Data Services, and specifically the IRIS Data Management Center, were
343 used for access to waveforms, related metadata, and/or derived products used in this study.
344 IRIS Data Services are funded through the Seismological Facilities for the Advancement of
345 Geoscience and EarthScope (SAGE) Proposal of the National Science Foundation under
346 Cooperative Agreement EAR-1261681. Data for the CD-CAT experiment
347 (https://doi.org/10.7914/SN/YB_2013) are available from the IRIS Data Management Center
348 at <http://www.iris.edu/hq/>. Tuna Eken acknowledge financial support from Alexander von
349 Humboldt Foundation (AvH) towards computational and peripherals resources.

350 *References*

351 Abercrombie, R.E.: Earthquake source scaling relationships from -1 to 5 ML using
352 seismograms recorded at 2.5-km depth, J. geophys. Res., 100(B12), 24 015–24 036,
353 1995.

354 Aki, K., and Chouet., B.: Origin of coda waves: Source, attenuation, and scattering effects, J.
355 Geophys. Res. 80, 3322–3342, 1975.

356 Ates, A., Kearey, P., and Tufan, S.: New gravity and magnetic anomaly maps of Turkey:
357 Geophysical Journal International, v. 136, p. 499–502, 1999.

358 Bozkurt, E.: Neotectonics of Turkey—A synthesis: Geodinamica Acta, v. 14, p. 3–30, 2001.

359 Bulut, F., Bohnhoff, M., Eken, T., Janssen, C., Kılıç, T., and Dresen, G.: The East Anatolian
360 fault zone: Seismotectonic setting and spatiotemporal characteristics of seismicity based
361 on precise earthquake locations: Journal of Geophysical Research, v. 117, B07304,
362 <https://doi.org/10.1029/2011JB008966>, 2012.

363 Çemen, I., Göncüoğlu, M.C., and Dirik, K.: Structural evolution of the Tuz Gölü basin in central
 364 Anatolia, Turkey: *Journal of Geology*, v. 107, p. 693–706, <https://doi.org/10.1086/314379>, 1999.
 365
 366 Çubuk Y, Yolsal-Çevikbilen S, Taymaz, T.: Source parameters of the 20052008 Balıkesir (central Turkey) earthquakes: Implications for the internal deformation of the Anatolian
 367 plate. *Tectonophysics* 635(Supplement C) :125 – 153, 2014.
 368
 369 Delph, J.R., Biryol, C.B., Beck, S.L., Zandt, G., and Ward, K.M.: Shear wave velocity structure
 370 of the Anatolian plate: Anomalously slow crust in southwestern Turkey: *Geophysical Journal International*, v. 202, p. 261–276, 2015.
 371
 372 Eken, T., Mayeda, K., Hofstetter, A., Gök, R., Orgülü, G. and Turkelli, N.: An application of the
 373 coda methodology for moment-rate spectra using broadband stations in Turkey.
 374 *Geophys. Res. Lett.*, 31, L11609, 2004.
 375 Eulenfeld, T. and Wegler, U.: Measurement of intrinsic and scattering attenuation of shear
 376 waves in two sedimentary basins and comparison to crystalline sites in Germany,
 377 *Geophys J Int.*, 205(2):744-757, 2016.
 378 Eulenfeld, T. and Wegler, U.: Crustal intrinsic and scattering attenuation of high-frequency
 379 shear waves in the contiguous United States. *J Geophys. Res.*, 122, 2017.
 380 Favreau, P., and Archuleta, R.J.: Direct seismic energy modelling and application to the 1979
 381 Imperial Valley earthquake, *Geophys. Res. Lett.*, 30, 1198, 2003.
 382 Fichtner, A., Saygin, E., Taymaz, T., Cupillard, P., Capdeville, Y., and Trampert, J.: The deep
 383 structure of the North Anatolian Fault Zone, *Earth Planet. Sc. Lett.*, 373, 109–117,
 384 2013a.
 385 Fichtner, A., Trampert, J., Cupillard, P., Saygin, E., Taymaz, T., Capdeville, Y., and Villasenor,
 386 A.: Multiscale full waveform inversion, *Geophys. J. Int.*, 194, 534–556,
 387 [doi:10.1093/gji/ggt118](https://doi.org/10.1093/gji/ggt118), 2013b.

388 Gaebler, P.J., Eulenfeld, T. & Wegler, U.: Seismic scattering and absorption parameters in the
 389 W-Bohemia/Vogtland region from elastic and acoustic radiative transfer theory,
 390 Geophys. J. Int., 203(3), 1471–1481, 2015.

391 Gaebler, P.J., Eken, T., Bektaş, H.Ö, Eulenfeld, T., Wegler, U., Taymaz, T.: Imaging of Shear
 392 Wave Attenuation Along the Central Part of the North Anatolian Fault Zone, Turkey,
 393 submitted to the Journal of Seismology, 2018.

394 Gök, R., Kaviani, A., Matzel, E. M., Pasyanos, M. E., Mayeda, K., Yetirmishli, G., El-
 395 Hussain, I., Al-Amri, A., Al-Jeri, F., Godoladze, T., Kalafat, D., Sandvol, E. A., and
 396 Walter, W.R.: Moment Magnitudes of Local/Regional Events from 1D Coda
 397 Calibrations in the Broader Middle East Region. Bull Seismol Soc Am., 106(5):1926-
 398 1938, 2016.

399 Gusev, A.A. & Abubakirov, I.R.: Simulated envelopes of non-isotropically scattered body
 400 waves as compared to observed ones: another manifestation of fractal heterogeneity,
 401 Geophys. J. Int., 127(1), 49–60, 1996.

402 Hanks, T.C. and Kanamori, H.: A moment magnitude scale, J. Geophys., Res., 84, 2348–
 403 2350, 1979.

404 Higgins, M., Schoenbohm, L.M., Brocard, G., Kaymakci, N., Gosse, J.C., and Cosca, M.A.:
 405 New kinematic and geochronologic evidence for the Quaternary evolution of the
 406 Central Anatolian fault zone (CAFZ), Tectonics, v. 34, pages, 2118- 2141, 2015.

407 Izgi, G., Eken, T., Gaebler, P., and Taymaz, T.: Frequency-Dependent Shear Wave
 408 Attenuation Along the Western Part of the North Anatolian Fault Zone, Geophysical
 409 Research Abstracts, Vol. 20, EGU2018-629-2, 2018.

410 Kaymakci, N. Inceöz, M. Ertepinar, P.: 3D architecture and Neogene evolution of the Malatya
 411 Basin: inferences for the kinematics of the Malatya and Ovacik Fault Zones. Turkish
 412 Journal of Earth Sciences, 15, 123-154, 2006.

413 Kwiatek, G., Plenkers, K. & Dresen, G.: 2011. Source parameters of pico-seismicity recorded
 414 at Mponeng Deep Gold Mine, South Africa: implications for scaling relations, *Bull.*
 415 *seism. Soc. Am.*, 101(6), 2592–2608, 2011.

416 Malagnini, L., Mayeda, K., Akinci, A., and Bragato, P. L.: Estimating absolute site effects,
 417 *Bull. Seismol. Soc. Am.* 94, no. 4, 1343–1352, 2004.

418 Mayeda, K., and Walter, W.R.: Moment, energy, stress drop, and source spectra of western
 419 United States earthquakes from regional coda envelopes, *J. Geophys. Res.* 101,
 420 11,195–11,208, 1996.

421 Mayeda, K., Hofstetter, A., O’Boyle, J.L., and Walter, W.R.: Stable and transportable
 422 regional magnitudes based on coda-derived moment-rate spectra, *Bull. Seismol. Soc.*
 423 *Am.* 93, 224–239: 2003.

424 Morasca, P., Mayeda, K., Malagnini, L. and Walter, W.R.: Coda and direct-wave attenuation
 425 tomography in northern Italy, *Bull Seismol Soc Am.*, v. 98, pages, 1936-1946, 2004.

426 Morasca, P., Mayeda, K., Gök, R., Phillips, W.S., and Malagnini, L.: Coda-derived source
 427 spectra, moment magnitudes and energy-moment scaling in the western Alps,
 428 *Geophys. J. Int.*, 160, 263–275, 2008.

429 Paasschens, J.: Solution of the time-dependent Boltzmann equation, *Phys. Rev. E*, 56(1),
 430 1135–1141, 1997.

431 Portner, D.E., Delph, J.R., Biryol, C.B., Beck, S.L., Zandt, G., Özacar, A.A., Sandvol, E., and
 432 Türkelli, N.: Subduction termination through progressive slab deformation across
 433 Eastern Mediterranean subduction zones from updated P-wave tomography beneath
 434 Anatolia, *Geosphere*, 14(3): 907-925, 2018.

435 Przybilla, J. and Korn, M.: Monte Carlo simulation of radiative energy transfer in continuous
 436 elastic random mediathree-component envelopes and numerical validation. *Geophys J*
 437 *Int* , 173(2):566-576, 2008.

438 Rautian, T.G. & Khalturin, V.I.: The use of the coda for determination of the earthquake
 439 source spectrum, *Bull. Seism. Soc. Am.*, 68(4), 923–948, 1978.
 440 Sato, H. and Fehler, M.C.: *Seismic Wave Propagation and Scattering in the Heterogeneous*
 441 *Earth*, Springer-Verlag, New York, 1998.
 442 Sato, H., Fehler, M.C. & Maeda, T. *Seismic Wave Propagation, and Scattering in the*
 443 *Heterogeneous Earth*, 2nd edn, Springer: 2012.
 444 Sens-Schönfelder, C. and Wegler, U.: Radiative transfer theory for estimation of the seismic
 445 moment. *Geophys J Int*, 167(3):1363-1372.
 446 Şengör, A.M.C., Tüysüz, O., İmren, C., Sakıncı, M., Eyidoğan, H., Görür, N., Le Pichon, X.,
 447 and Rangin, C.: The North Anatolian fault: A new look: *Annual Review of Earth and*
 448 *Planetary Sciences*, v. 33, p. 37–112, 2005.
 449 Taymaz, T., Jackson, J., Westaway, R.: Earthquake mechanisms in the Hellenic Trench near
 450 Crete. *Geophys. J. Int.* 102, 695–731, 1990.
 451 Taymaz, T., Westaway, R., Reilinger, R.: Active faulting and crustal deformation in the
 452 eastern Mediterranean Region. *Spec. Issue Tectonophys.* 391 (1-4), 1–9. [http://](http://dx.doi.org/10.1016/j.tecto.2004.07.005)
 453 dx.doi.org/10.1016/j.tecto.2004.07.005, 2004.
 454 Yoo, S.-H., Rhie, J., Choi, H.-S., and Mayeda, K.: Coda-derived source parameters of
 455 earthquakes and their scaling relationships in the Korean Peninsula, *Bull. Seismol.*
 456 *Soc. Am.*, 101, 2388–2398, 2011.
 457 Wu, R. and Aki, K.: The fractal nature of the inhomogeneities in the lithosphere evidenced
 458 from seismic wave scattering, *Pure appl. Geophys.*, 123(6), 805–818, 1985.
 459 Zeng, Y., Su, F. and Aki, K.: Scattering wave energy propagation in a random isotropic
 460 scattering medium: 1. Theory, *J. Geophys. Res.*, 96(B1), 607–619, 1991.
 461
 462

463 *Figure Captions*

464 Figure 1. Major tectonic features of Turkey and its adjacentsç The plate boundary data used
465 here is taken from Bird (2003). Subduction zones are black, continental transform faults are
466 red, continental rift boundaries are green, and spreading ridges boundaries are yellow. NAFZ,
467 EAFZ, and DSFZ are the North Anatolian Fault, East Anatolian Fault, and the Dead Sea fault,
468 respectively.

469
470 Figure 2. Epicentral distribution of all local events selected from the study area in the KOERI
471 catalogue. Gray circles represent earthquakes with poor quality that are not considered for the
472 current study while black indicates the location of local events with good quality. Red circles
473 among these events are 487 events used in coda wave inversion since they are successful at
474 passing quality criteria of further pre-processing procedure.

475
476 Figure 3. An example from the inversion procedure explained in chapter 3. Here coda
477 envelope fitting optimization is performed on band-pass filtered (8-16Hz) digital recordings
478 of an earthquake (2014 April 09, M_w -coda3.2) extracted for 7 seismic stations that operated
479 within the CD-CAT array. Large panel at the lower left-hand side displays the error function ϵ
480 as a function of g_0 . Thick blue cross here represent the optimal value of $g = g_0$. Other small
481 panels at upper and right-hand side show the least- squares solution of the weighted linear
482 equation system for the first 6 guesses and optimal guess for g_0 . There dots and gray curves
483 indicate the ratio between energy (E^{obs}) and the Green's function (G) obtained for direct S-
484 waves and observed envelopes at various stations, respectively. Please notice that during this
485 optimization process envelopes are corrected for the obtained site corrections R. The slope of
486 linear curve at each small panel yields $-b$ and while its intercept W are the intrinsic

or 4-8 Hz?

English

i.e.,

What attenuation are you looking about?

487 attenuation and source related terms at the right-hand side of equation 4 part of the right-hand
488 side of the equation system.

English

489
490 Figure 4. a) Results of the inversion of the 2014-April-09, M_W -coda3.2 earthquake: Sample
491 fits between observed and calculated energy densities in the frequency band 0.5–1.0 Hz are
492 given for 6 different stations (see upper right corner for event ID, station name, and distance
493 to hypocenter). Note that light blue curves represent observed envelope. Smoothed observed
494 calculated envelopes in each panel are presented by blue and red curves, respectively. Blue
495 and red dots exhibit location of the average value for observed and calculated envelopes
496 within the S-wave window, respectively. b) The same as in (a) obtained in the frequency band
497 4.0–8.0 Hz.

→ Where is the figure discussed in the text?

499 Figure 5. All individual observed (black squares) and predicted (gray curve) source
500 displacement spectra observed at 72 stations from 487 local earthquakes in central Anatolia.

502 Figure 6: Scatter plot between local magnitudes (M_L) of analyzed events with coda waves-
503 derived magnitudes (M_W -coda) of the same events. The outcome of a linear regression
504 analysis yielded an empirical formula (e.g. Eq. 9) to identify the overall agreement represented
505 by gray straight line. Yellow and red dashed lines indicate upper and lower limit of linearly
506 fitting to that scatter.

508 Figure 7: Same scatter plot displayed in Fig. 6 color coded by estimated high-frequency fall-
509 off parameter for each inverted event.

English

Figure 6 and 7 might be merged

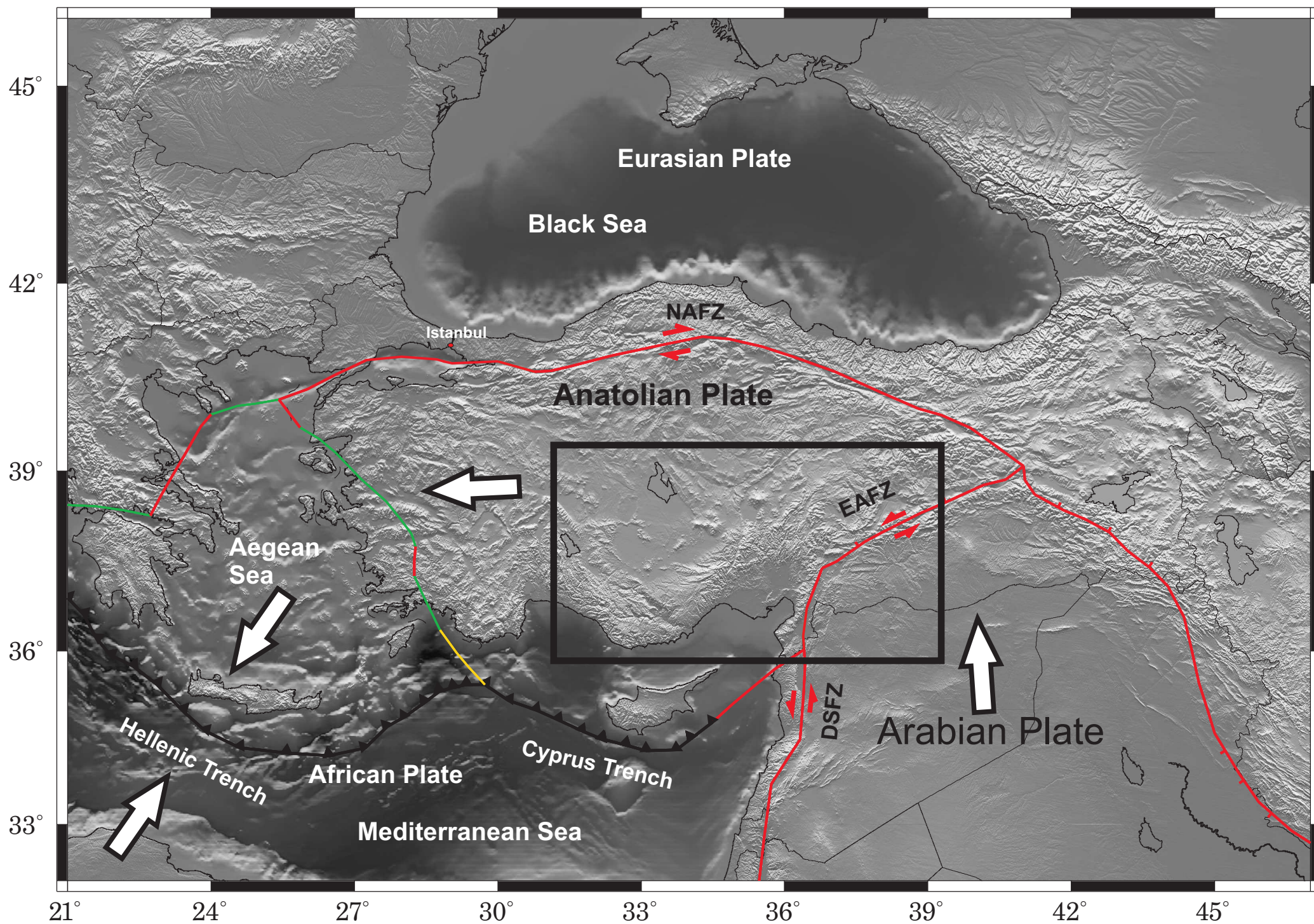


Fig. 1

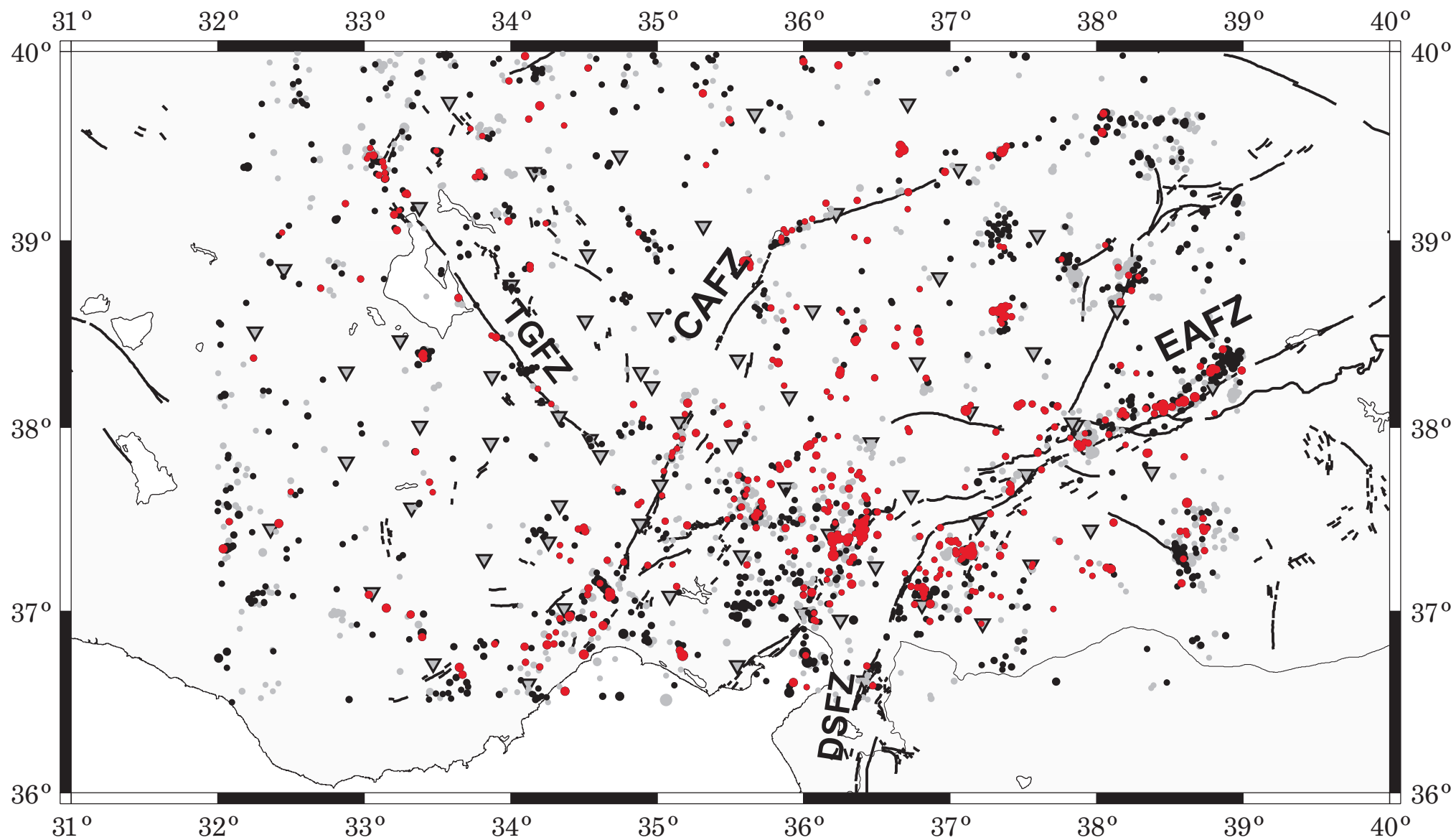


Fig. 2

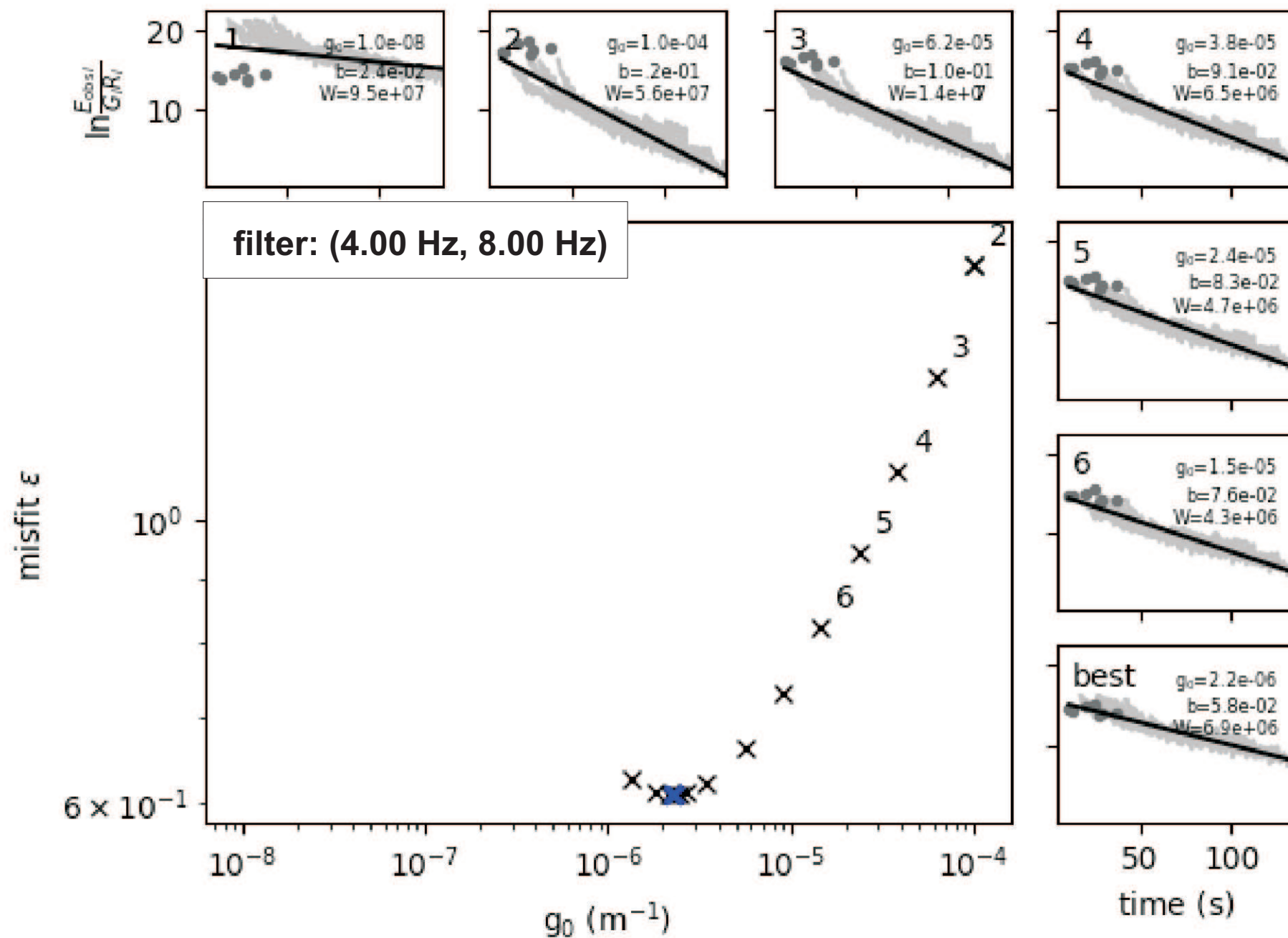
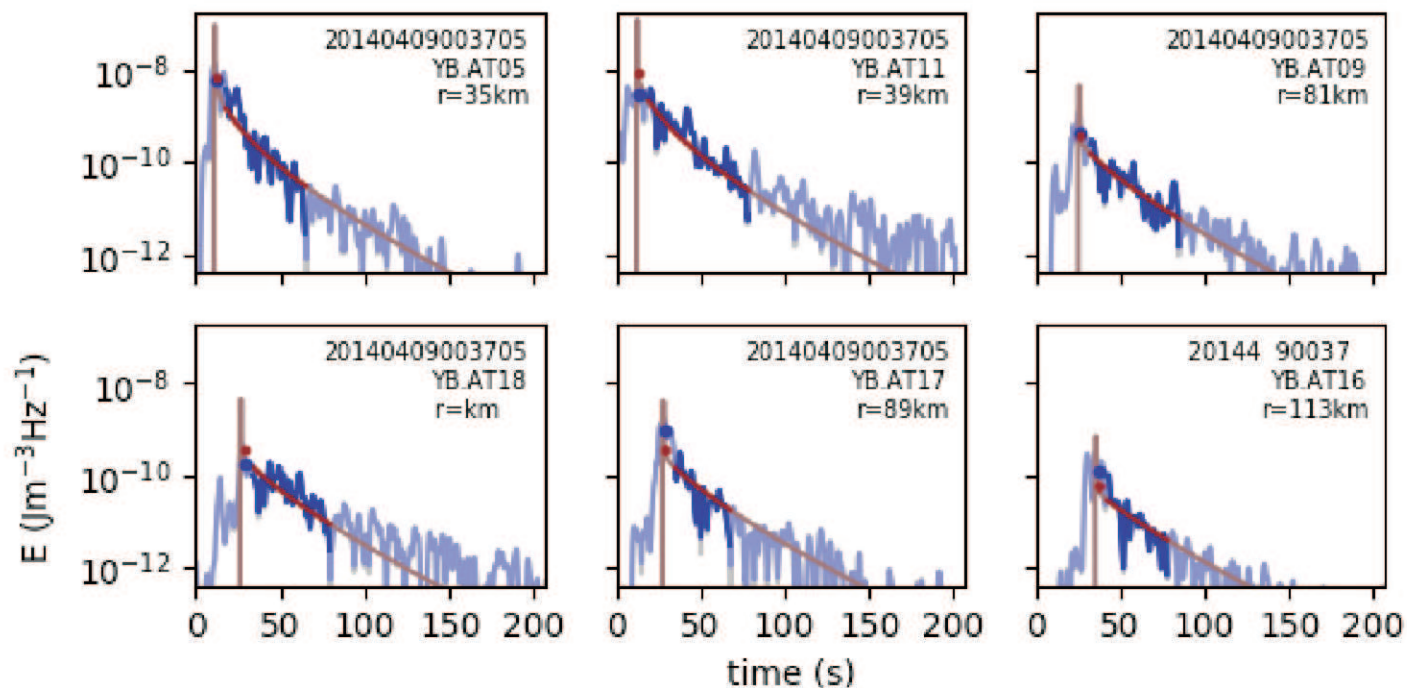


Fig. 3

filter: (0.50Hz, 1.00Hz)

a)



filter: (4.00Hz, 8.00Hz)

b)

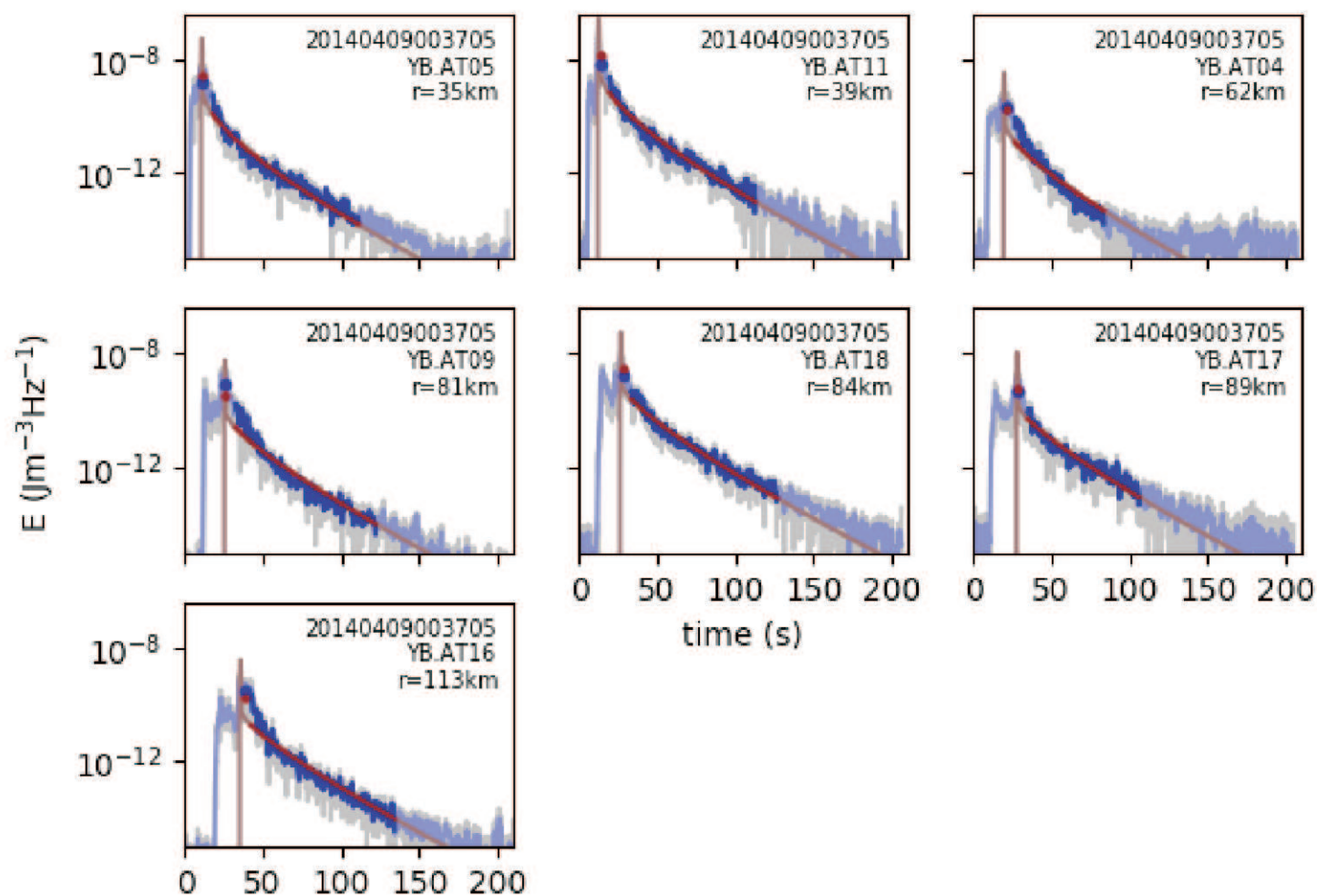


Fig. 4

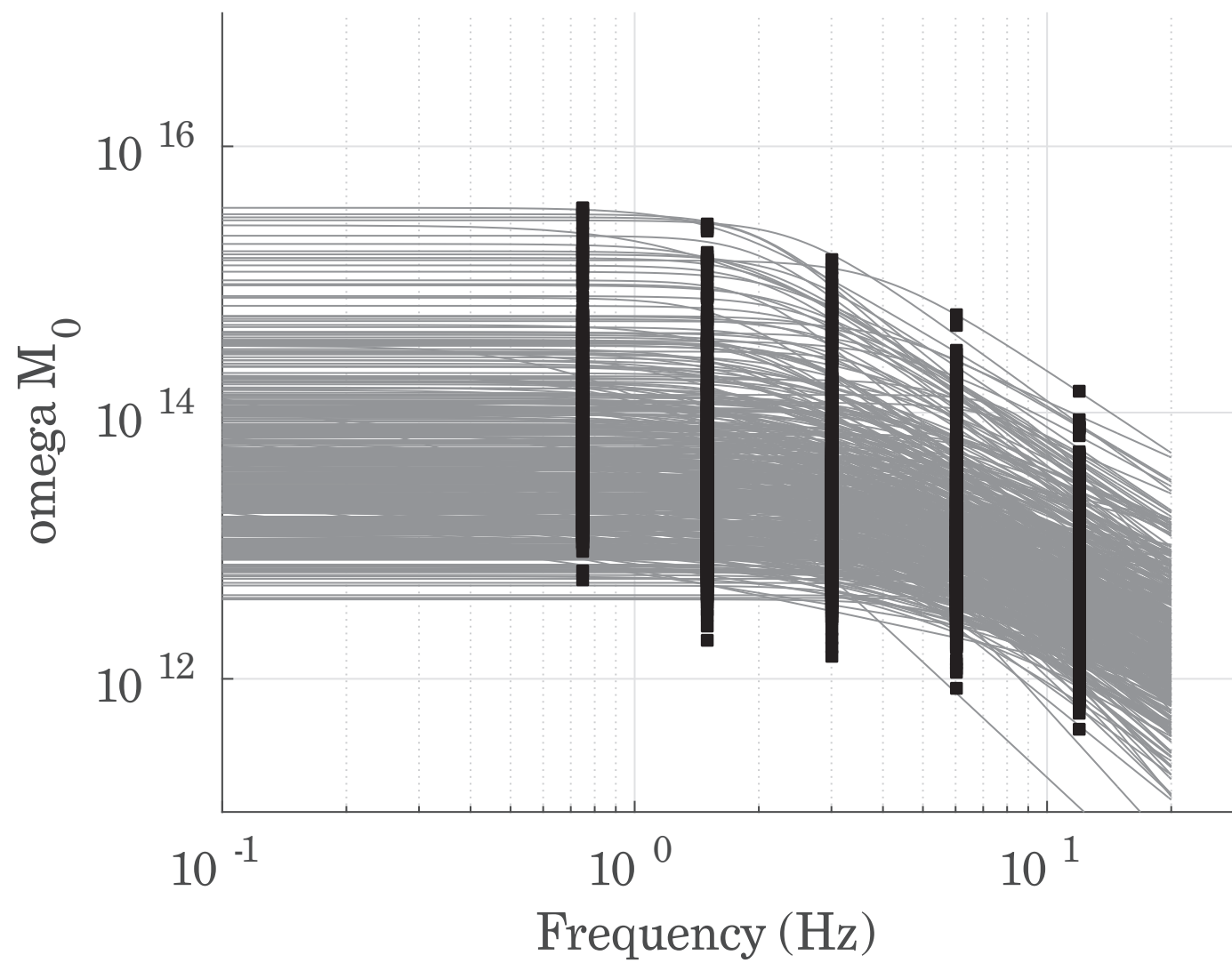


Fig. 5

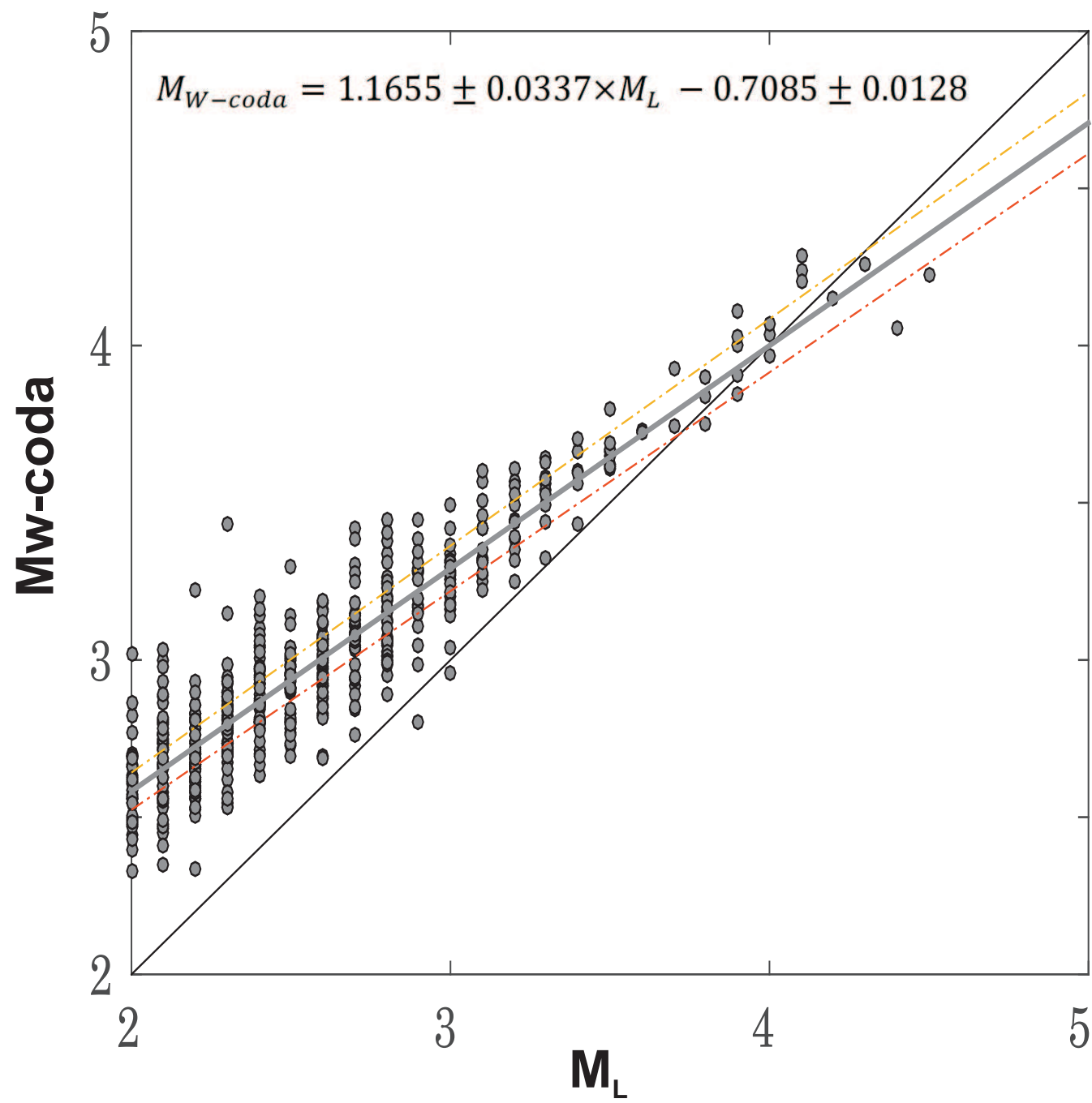


Fig. 6

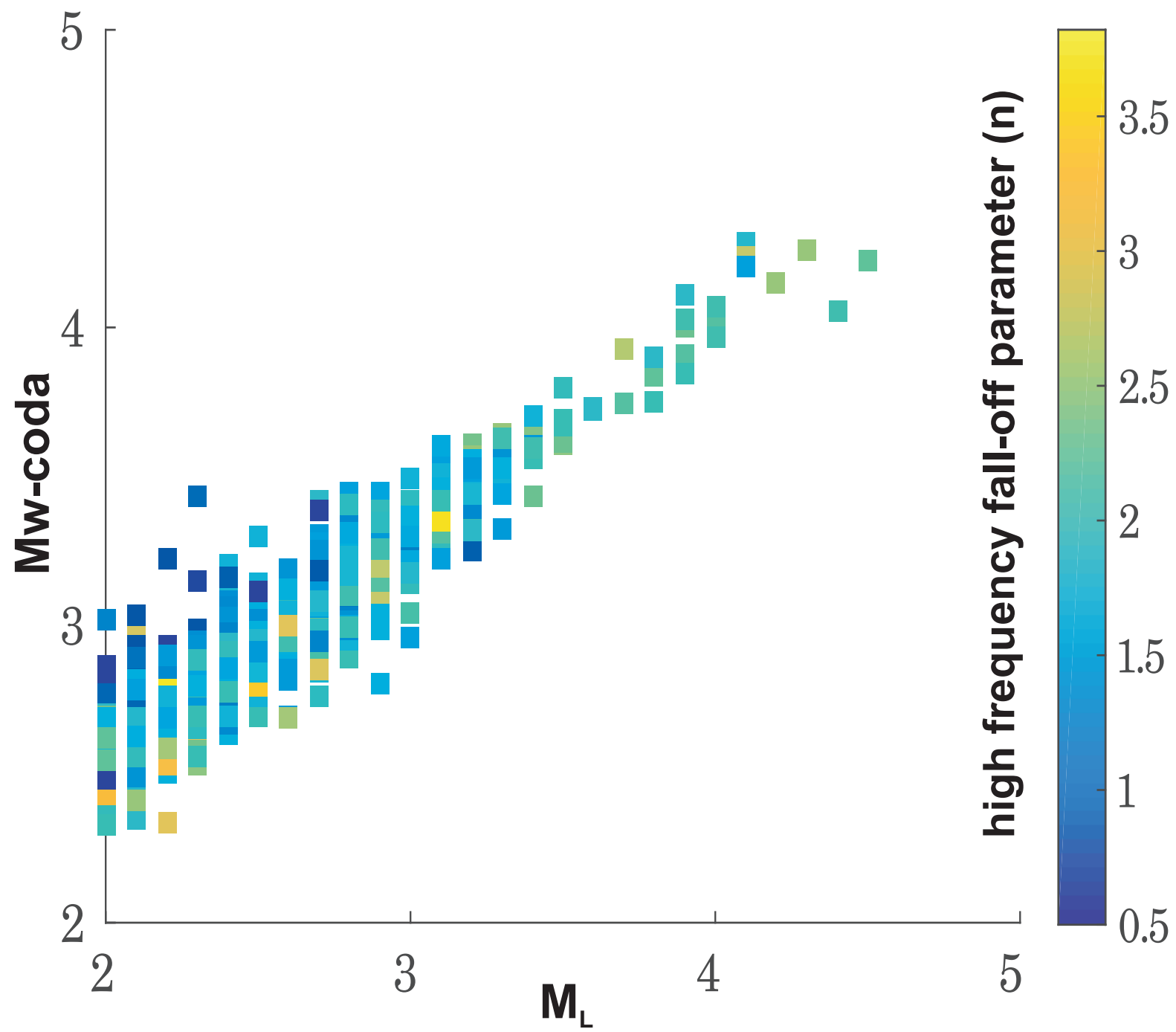


Fig. 7